

Classification

Physics Abstracts

61.30G — 47.20 — 61.30 — 62.10

## Field-induced transient periodic structures in nematic liquid crystals : the splay Frederiks transition

A. J. Hurd (\*), S. Fraden, F. Lonberg and R. B. Meyer

Martin Fisher School of Physics, Brandeis University, Waltham, MA 02254, U.S.A.

*(Reçu le 8 octobre 1984, accepté le 13 février 1985)*

**Résumé.** — Une belle texture en bandes apparaît souvent comme réponse initiale d'un cristal liquide nématique uniformément aligné à l'application soudaine d'un champ magnétique d'orientation différente. La structure de l'instabilité dépend de l'élasticité et de la viscosité anisotrope du cristal liquide, de l'amplitude du champ et, de façon importante, des conditions aux limites imposées par la cellule contenant l'échantillon. Nous avons étudié la géométrie dans laquelle le champ magnétique est perpendiculaire aux parois parallèles de la cellule contenant un cristal liquide nématique planaire composé d'une suspension de particules de virus de la mosaïque du tabac. Dans cette géométrie, des domaines en bandes parallèles s'établissent dans deux directions. Leur longueur d'onde et l'angle qu'ils forment avec l'orientation initiale du directeur dépendent du champ magnétique. La distorsion initiale apparaît sous forme de carreaux délimités par deux séries de lignes parallèles. Nous avons analysé cette structure par une analyse de stabilité hydrodynamique linéaire développée de deux façons. Nous présentons tout d'abord une analyse générale des équations du mouvement et nous déterminons l'angle et la longueur d'onde employant des valeurs raisonnables pour les paramètres de la matière et supposant des parois libres. Ensuite une simple théorie basée sur des arguments d'énergie est présentée dans la limite de très longues molécules. Elle reproduit les aspects essentiels des échantillons de virus de la mosaïque du tabac. Finalement une investigation des effets de parois rigides dans un cas simplifié montre qu'ils n'affectent pas les conclusions tirées pour le cas des parois libres.

**Abstract.** — A beautiful striped texture is often observed as the initial response of a uniformly aligned nematic liquid crystal to a suddenly applied reorienting field. The structure of the instability depends on the elastic and viscous anisotropy of the liquid crystal, the field strength, and in an important way on the boundary conditions imposed by the sample cell. We have studied the geometry in which a magnetic field is applied normal to a parallel-plate cell containing a planar-aligned liquid crystal composed of suspended tobacco mosaic virus particles. In this geometry, parallel striped domains develop in two directions with a field-dependent wavelength and angle relative to the initial director. The initial distortion appears as a cross-hatched pattern of intersecting sets of parallel lines. We have analysed the pattern by a linear hydrodynamic stability analysis in two ways: First, a general analysis of the equations of motion is presented which describes the angle and wavelength with reasonable values for the material parameters and assuming free boundary conditions. Second, a simple theory based on energetics for the limit of very long molecules is given, which reproduces the essential features of the tobacco mosaic virus samples. Finally the effects of rigid boundaries are investigated for a simplified case and are found not to alter the conclusions drawn for free boundaries.

### 1. Introduction.

It is surprising that field-induced transient hydrodynamic instabilities in nematic liquid crystals have gone relatively unnoticed in spite of the fact that the Frederiks transition is one of the most important experimental tools for measuring liquid crystal material parameters. In the usual Frederiks transition, a field is applied to a uniformly aligned sample in such a way that the director tends to realign perpendicular

to its original direction; the final angle of the director is that at which the field torque is balanced locally by the elastic restoring torque transmitted through the liquid crystal from the anchored boundaries. Although the final alignment state is uniform in the plane of the sample, the path to that state often involves a spatially periodic, transient instability in which adjacent domains of the sample rotate in opposite senses. It is this initial response that gives rise to the striped textures that have been largely overlooked. Here we present the results of our experimental and theoretical studies of field-induced stripes in the splay-bend Frederiks transition geometry. In a pre-

(\*) Permanent address : Sandia National Laboratories, Albuquerque, NM 87185, U.S.A.

vious paper we examined the twist-bend geometry [1, 2].

The fast response of ordinary thermotropic nematics may have prevented the occurrence or observation of the transient stripes. When they do occur, they anneal away rather quickly in these materials; it is with slower lyotropic systems that the beautiful patterns become obvious. Indeed, the growing interest in lyotropics has led to a number of recently reported observations [1-4] although the earliest reports were in MBBA [5, 6].

The coupling between flow and reorientation leading to these effects was described by Guyon, *et al.* [5] who also studied the splay-bend case. In this geometry the director, initially parallel to the walls of a thin cell (planar alignment), is suddenly forced to rotate toward the normal to the walls (homeotropic alignment) by an external field. Using fairly high fields relative to the critical field of the normal Frederiks transition, they found a system of regular stripes perpendicular to the initial director whose wavelength was field-dependent. This implies that the fluid flows and the director remain in a single plane, and so the analysis of the problem is somewhat simplified.

We have repeated these experiments with thinner, more manageable samples in relatively low magnetic fields using a lyotropic liquid crystal composed of tobacco mosaic virus (TMV) particles suspended in water, and we have found that the stripes are not always perpendicular to the initial director. Instead they can form at an acute angle on either side of the director. We have made similar observations on thin samples of MBBA. The implication is that the problem is not strictly two-dimensional: to explain the angled stripes, one must keep track of the flow and director fields in three dimensions.

In this paper we present such an analysis, based on the idea that the initial distortion is dominated by the fastest growing periodic modes. Following Guyon, these modes are found by solving for the maximum rate of growth as a function of wave vector  $\mathbf{k}$  from the three-dimensional equations of nematodynamics. Alternatively, the same dynamical information can be obtained from the balance between conservative and dissipative energy changes. Certain components of  $\mathbf{k}$  must be fixed to satisfy rigid boundary conditions, which is accomplished by combining modes with the same growth rate; for rigid boundaries, however, it appears from our analysis to be sufficient to discuss only the free-boundaries mode.

That a maximum in the growth rate exists at finite wave vector can be understood by the fact that the energy dissipation rate in a periodic distortion is characterized by an effective viscosity which is wave vector-dependent in general because director rotation and fluid velocity gradients are coupled in nematics and because the viscous properties are anisotropic. Shorter wavelength distortions tend to be of smaller effective viscosity owing to the cooperation between

director and velocity in spite of the fact that there are greater velocity gradients. At longer wavelengths the presence of boundaries becomes important tending to make the effective viscosity greater. Meanwhile a lower elastic energy favours modes of longer wavelengths, so unless it dominates, leading to a non-periodic response with  $\mathbf{k} = 0$ , a compromise is found at some intermediate  $\mathbf{k}$ . Hence, by incorporating components of rotation that do not directly lower the driving field energy, a smaller effective viscosity or a smaller elastic restoring force can be found by the system in order to maximize response rate. This is why the planar-to-homeotropic transition involves three-dimensional flows in general and why the stripes are oblique.

In section 2, the linearized equations of motion are derived from Euler-Lagrange mechanics and solved by Fourier transforms. The problem of satisfying boundary conditions exactly is discussed using the two-dimensional limit (no obliqueness in the stripes) of the planar-to-homeotropic case as an illustration. Certain features of the full three-dimensional equations, which are solved numerically for free boundary conditions, are shown graphically. In addition, the infinite chain limit is treated by appealing directly to energy conservation. The measurements with TMV are described in section 3 with a comparison to the dynamical theory in section 4. The results show the general trends in the mechanical anisotropy predicted for hard-rod liquid crystals.

## 2. Linearized equations.

In the following development, the nematic liquid crystal is assumed initially to be uniformly aligned parallel to glass plates spaced by a distance  $d$ , and a magnetic field is applied normal to the plates. Letting the  $z$  axis be along the field and the  $x$  axis along the initial director  $\hat{\mathbf{n}}$  as in figure 1, the Lagrangian density for small displacements and ignoring inertial terms

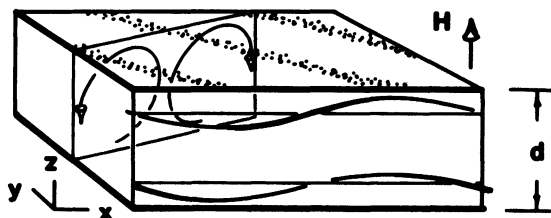


Fig. 1. — Reorientational instability in nematic liquid crystals. The sample is constrained between two plates spaced by a thickness  $d$ . A magnetic field is suddenly applied normal to the cell along the  $z$  direction giving rise to a transient periodic structure that appears under crossed polarizers as oblique stripes in the  $x$ - $y$  plane. The director lines are helicoidal, rotating in opposite sense on either side of the midplane. The flow lies in some plane across the stripes and is characteristic of convection cells.

is [7]

$$\begin{aligned}
 &= \frac{1}{2} \Delta\chi (\mathbf{H} \cdot \mathbf{n})^2 - \frac{1}{2} K_1 (\nabla \cdot \mathbf{n})^2 - \frac{1}{2} K_2 (\mathbf{n} \cdot \nabla \times \mathbf{n})^2 - \frac{1}{2} K_3 (\mathbf{n} \times \nabla \times \mathbf{n})^2 - \mathbf{u} \cdot \nabla p \\
 &= \frac{1}{2} \Delta\chi H_z^2 n_z^2 - \frac{1}{2} K_1 (n_{y,y} + n_{z,z})^2 - \frac{1}{2} K_2 (n_{z,y} - n_{y,z})^2 - \frac{1}{2} K_3 (n_{x,x}^2 + n_{z,x}^2) - u_x p_{,x} - u_y p_{,y} - u_z p_{,z} \quad (1)
 \end{aligned}$$

where  $\mathbf{n}$  is the director,  $\mathbf{u}$  is the displacement vector,  $p$  is the pressure,  $\mathbf{H}$  is the magnetic field,  $\Delta\chi$  is the diamagnetic susceptibility anisotropy and  $K_1$ ,  $K_2$  and  $K_3$  are the splay, twist and bend elastic constants, respectively. Spatial derivatives are indicated by subscripts following a comma. The last term in equation (1) corresponds to work done by fluid displacements against a pressure gradient ; its inclusion serves to reproduce the traditional equations of nematodynamics.

Rayleigh's dissipation function for a nematic has been derived recently by Vertogen [8], which for the present geometry is

$$\begin{aligned}
 &= v_1 v_{x,x}^2 + \frac{1}{2} \eta_b (v_{x,y}^2 + v_{x,z}^2) + \frac{1}{2} \eta_c (v_{y,x}^2 + v_{z,x}^2) + \eta_a (v_{y,y}^2 + v_{z,z}^2) + \frac{1}{2} \eta_a (v_{y,z} + v_{z,y})^2 + \\
 &\quad + \frac{1}{2} \gamma_1 (\dot{n}_y^2 + \dot{n}_z^2) + \eta_4 (v_{x,y} v_{y,x} + v_{x,z} v_{z,x}) + \alpha_2 (v_{y,x} \dot{n}_y + v_{z,x} \dot{n}_z) + \alpha_3 (v_{x,y} \dot{n}_y + v_{x,z} \dot{n}_z), \quad (2)
 \end{aligned}$$

where  $\mathbf{v} = \dot{\mathbf{u}}$  and the five basic viscosities are taken to be the Miesowicz shear viscosities,  $\eta_a$ ,  $\eta_b$  and  $\eta_c$ , along with  $v_1$  (elongational flow) and  $\gamma_1$  (molecular rotation without flow). The coupling viscosities,  $\eta_4$ ,  $\alpha_2$  and  $\alpha_3$ , are related to these by

$$\begin{aligned}
 \eta_4 &= \frac{1}{2} (\eta_b + \eta_c - \gamma_1) \\
 \alpha_2 &= \frac{1}{2} (\eta_b - \eta_c - \gamma_1) \\
 \alpha_3 &= \frac{1}{2} (\eta_b - \eta_c + \gamma_1).
 \end{aligned}$$

By a suitable generalization of Vertogen's work, the Euler-Lagrange equations of motion are [9]

$$\frac{d}{dt} \frac{\partial L}{\partial \dot{q}_i} - \frac{\partial L}{\partial q_i} + \sum_k \frac{d}{dx_k} \frac{\partial L}{\partial \dot{q}_{i,k}} = - \frac{\partial R}{\partial \dot{q}_i} + \sum_k \frac{d}{dx_k} \frac{\partial R}{\partial \dot{q}_{i,k}}. \quad (3)$$

Here  $q_i$  is a generalized coordinate of which there are five : the three components of  $\mathbf{u}$  and the two transverse components of  $\mathbf{n}$ . Taking  $q_i = u_i$  yields the linear momentum equations

$$0 = - p_{,x} + \alpha_3 (\dot{n}_{y,y} + \dot{n}_{z,z}) + 2 v_1 v_{x,xx} + \eta_4 (v_{y,xy} + v_{z,xz}) + \eta_b (v_{x,yy} + v_{x,zz}) \quad (4a)$$

$$0 = - p_{,y} + \alpha_2 \dot{n}_{y,x} + \eta_c v_{y,xx} + \eta_4 v_{x,yy} + \eta_a (v_{z,yz} + v_{y,zz} + 2 v_{y,yy}) \quad (4b)$$

$$0 = - p_{,z} + \alpha_2 \dot{n}_{z,x} + \eta_c v_{z,xx} + \eta_4 v_{x,zx} + \eta_a (v_{y,zy} + v_{z,yy} + 2 v_{z,zz}). \quad (4c)$$

The torque equations are similarly found by taking  $q_i = n_i$ ,

$$\gamma_1 \dot{n}_y = - \alpha_2 v_{y,x} - \alpha_3 v_{x,y} + K_1 (n_{y,yy} + n_{z,zy}) + K_2 (n_{y,zz} - n_{z,yz}) + K_3 n_{y,xx} \quad (5a)$$

$$\gamma_1 \dot{n}_z = - \alpha_2 v_{z,x} - \alpha_3 v_{x,z} + K_1 (n_{y,yz} + n_{z,zz}) + K_2 (n_{z,yy} - n_{y,zy}) + K_3 n_{z,xx} + \Delta\chi H_z^2 n_z. \quad (5b)$$

Finally, fluid incompressibility requires

$$0 = v_{x,x} + v_{y,y} + v_{z,z}. \quad (6)$$

Using the fact that  $\nabla \times (\nabla p) = 0$ , the pressure can be eliminated, and after a Fourier transform, the velocity

$v_x$  can be eliminated readily using equation (6), leaving four equations in four unknown amplitudes,

$$0 = 0 \quad -g_1(ik_x n_z) + f_1 v_y + f_{2z} v_z, \quad (7)$$

$$0 = -g_1(ik_x n_y) + 0 + f_{2y} v_y + f_1 v_z, \quad (8)$$

$$0 = -g_2(ik_x n_y) - g_3(ik_x n_z) + 0 + f_3 v_z, \quad (9)$$

$$0 = -g_{4z}(ik_x n_y) - g_5(ik_x n_z) + f_3 v_y + 0, \quad (10)$$

where

$$\begin{aligned} g_1 &= \alpha_2 k_1^2 s, \\ g_2 &= k_y k_z [(K_1 - K_2) k_1^2 - \alpha_3 k_2^2], \\ g_3 &= g_{4y} + \Delta\chi H_z^2 (\alpha_3 k_z^2 - k_1^2), \\ g_{4y} &= (\alpha_2 k_x^2 + \gamma_1 s) k_1^2 + \alpha_3 k_y^2 k_3^2, \\ g_{4z} &= (\alpha_2 k_x^2 + \gamma_1 s) k_1^2 + \alpha_3 k_z^2 k_3^2, \\ g_5 &= k_y k_z (g_2 + \alpha_3 \Delta\chi H_z^2), \\ f_1 &= k_y k_z k_B^2, \\ f_{2y} &= k_1^2 k_c^2 + k_B^2 k_y^2, \\ f_{2z} &= k_1^2 k_c^2 + k_B^2 k_z^2, \\ f_3 &= \alpha_2 k_1^2 k_x^2, \\ k_1^2 &= -\alpha_2 k_x^2 + \alpha_3 (k_y^2 + k_z^2), \\ k_2^2 &= K_3 k_x^2 + K_1 (k_y^2 + k_z^2), \\ k_3^2 &= K_3 k_x^2 + K_2 (k_y^2 + k_z^2), \\ k_B^2 &= \alpha_2 (\eta_b + \eta_c - \eta_a - \gamma_1 - 2\nu_1) k_x^2 + \eta_b (k_y^2 + k_z^2) - \alpha_3 k_c^2, \\ k_c^2 &= \eta_c k_x^2 + \eta_a (k_y^2 + k_z^2). \end{aligned}$$

Here  $s$  is the rate of growth of the mode whose time dependence is assumed to be  $\exp(st)$ . Further elimination of field amplitudes is possible but not particularly fruitful for numerical analysis.

**3.1 CHARACTERISTIC EQUATION.** — A necessary condition for a solution to exist is that the determinant of the coefficients in equations (7-10) must vanish. The resulting characteristic equation or dispersion relation is quadratic in the growth rate  $s$  and of the sixth power in each of  $k_x^2$ ,  $k_y^2$  and  $k_z^2$ .

$$\begin{vmatrix} 0 & -g_1 & f_1 & f_{2z} \\ -g_1 & 0 & f_{2y} & f_1 \\ -g_2 & -g_3 & 0 & f_3 \\ -g_{4z} & -g_5 & f_3 & 0 \end{vmatrix} = 0 \quad (11)$$

The unstable modes must have a real and positive growth rate, and since they are observed to be spatially periodic in the  $x$  and  $y$  directions they must have real wave vector components  $k_x$  and  $k_y$ .

Considered as a function of  $k_z^2$  then, the characteristic equation is a sixth-order polynomial with six independent roots; therefore there are six independent modes for a given rate of growth that satisfy the equations of motion.

**2.2 BOUNDARY CONDITIONS AND SYMMETRY.** — It is difficult to satisfy rigid boundary conditions exactly for the three-dimensional velocity and director fields.

The complexity of the problem tends to obscure the essential physics that is responsible for the striped patterns; therefore, only the free-boundaries case will be treated in detail. This approach will be justified in subsequent discussions comparing exact rigid-boundary results to free-boundary results.

Physically, the boundaries impose constraints on the allowed wave vectors normal to the cell. For the experiments we performed rigid boundaries were used,

$$\left. \begin{aligned} \mathbf{v} &= 0 \\ \mathbf{n} &= (1, 0, 0) \end{aligned} \right\} \text{ at } z = \pm d/2, \quad (12a)$$

but free boundaries are more tractable,

$$\left. \begin{aligned} v_{x,z} &= 0 \\ v_{y,z} &= 0 \\ v_z &= 0 \\ n_z &= 0 \end{aligned} \right\} \text{ at } z = \pm d/2. \quad (12b)$$

The solutions can be constructed to have definite symmetry in the  $z$  direction, even or odd, with respect to the midplane of the sample. (Symmetry in the  $x$ - $y$  plane is irrelevant to the growth rate by translational

invariance.) From equations (4) and (5) we see that  $v_x, v_y, n_y$  and  $p$  must have one type of symmetry (say odd) while  $v_z$  and  $n_z$  must have the other type (even),

$$\begin{aligned} v_x &= A \cos k_x x \cos k_y y \sin k_z z \\ v_y &= B \sin k_x x \sin k_y y \sin k_z z \\ v_z &= C \sin k_x x \cos k_y y \cos k_z z \\ n_y &= D \cos k_x x \sin k_y y \sin k_z z \\ n_z &= E \cos k_x x \cos k_y y \cos k_z z \\ p &= F \sin k_x x \cos k_y y \sin k_z z. \end{aligned} \quad (13)$$

One can easily verify that this solution satisfies the free boundary conditions, equation (12b), with  $k_z = \pi/d$ . The corresponding solution with odd  $z$ -symmetry for  $n_z$  must have  $k_z = 2\pi/d$  and can be shown to be slower; it is therefore always preempted by the even solution.

A few clarifying comments about the rigid-boundaries solution are in order. Since the characteristic equation is a sixth-order polynomial in  $k_z^2$ , the solutions to each field variable are composed of a sum of six independent modes corresponding to the six roots for  $k_z^2$ , some of which may be complex roots. By solving the boundary value problem exactly, we can determine an « effective sample thickness »  $d^* = \pi/k_z$  for each real root. The rate of growth can then be determined from the characteristic equation using

any of the roots for  $k_z$ . The maximum rate must be found by searching the  $k_x$ - $k_y$  plane.

It is this concept of an effective sample thickness that makes it easier to understand why the rigid and free boundaries give similar results. As we will show in the next section, which deals with a simplified case, the solution for rigid boundaries is a superposition of a simple mode resembling the free-boundaries solution (i.e. with  $k_z \approx \pi/d$  or  $d^* \approx d$ ) and other modes having complex wave vectors. In order to study the directions and wavelengths of the stripes, it is sufficient to consider only this simple mode since all the modes satisfy the same dispersion relation and it doesn't matter which one we choose to maximize the rate: each of them will produce the same wave vectors,  $k_x$  and  $k_y$ . Insofar as the simple mode resembles the free-boundaries solution with an effective thickness  $d^*$  nearly equal to the actual thickness  $d$ , we are justified in exploring the behaviour of the rigid-boundaries distortion as a function of applied magnetic field by numerically solving the free-boundaries problem, equation (11). These results are discussed in section 4.

**2.3 TWO-DIMENSIONAL CASE.** — As an illustration of the exact general procedure, the two-dimensional case, which Guyon *et al.* [5] analysed for free boundaries, will be analysed here for rigid boundaries. Setting  $v_y, n_y$  and  $k_y$  to zero, the characteristic equation becomes a cubic for  $k_z^2$ ,

$$(\eta_b K_1) k_z^6 + (\eta_b \xi + NK_1 k_x^2 - \alpha_2^2 s) k_z^4 + k_x^2 (N\xi + \eta_c K_1 k_x^2 + 2\alpha_2 \alpha_3 s) k_z^2 + k_x^4 (\eta_c \xi - \alpha_2^2 s) = 0 \quad (14)$$

where  $N = 2\eta_a - \eta_b - \eta_c + \gamma_1 - 2\nu_1$  and  $\xi = \gamma_1 s - \Delta\chi H_z^2 + K_3 k_x^2$ . Hence there are three roots  $q_j^2$  to  $k_z^2$ , one of which must be real. The solution for which  $n_z$  has even symmetry is

$$\begin{aligned} v_x &= \cos(k_x x) [A_1 \sin(q_1 z) + A_2 \sin(q_2 z) + A_3 \sin(q_3 z)] \\ v_z &= \sin(k_x x) [B_1 \cos(q_1 z) + B_2 \cos(q_2 z) + B_3 \cos(q_3 z)] \\ n_z &= \cos(k_x x) [C_1 \cos(q_1 z) + C_2 \cos(q_2 z) + C_3 \cos(q_3 z)]. \end{aligned} \quad (15)$$

From the torque equation and the incompressibility condition, equations (5b) and (6), the amplitudes  $B_j$  and  $C_j$  can be found in terms of the amplitudes  $A_j$  of the three independent modes.

$$B_j = -\frac{k_x}{q_j} A_j$$

$$C_j = \frac{D_j}{q_j} A_j$$

where

$$D_j = \frac{\alpha_2 k_x^2 - \alpha_3 q_j^2}{\xi + K_1 q_j^2}.$$

With these substitutions, the boundary conditions yield three equations in the three remaining ampli-

tudes whose coefficients must have a vanishing determinant. After some algebra, this condition becomes

$$0 = (D_3 - D_2) P_1 \tan P_1 + (D_3 - D_1) P_2 \tan P_2 + (D_1 - D_2) P_3 \tan P_3 \quad (16)$$

where  $P_j = q_j d/2$  can be complex. Thus, equation (16) and the three characteristic equations (one for each root) form a set of four nonlinear equations in four unknowns,  $q_1, q_2, q_3$  and the rate  $s$ , for a given wave vector  $k_x$ . The fastest growing mode must be found by searching through values for  $k_x$ .

The lowest order even solution involves an effective thickness  $d^* \approx d$  whereas the lowest order odd solution has  $d^* \approx \frac{1}{2}d$ . With this information, it can be shown from equation (14) that the odd solution

is always slower than the even one although both give stripes. The wavelength of the even solution should be the one that is observed.

For fields just above the Frederiks transition field, a spatially uniform realignment, similar to one previously studied [10], is possible and actually is faster than the striped mode. It must be treated separately as follows.

Assuming no variation in either the  $x$  or  $y$  directions, we have immediately  $v_z = 0$  and the equations of motion

$$0 = \frac{d}{dz}(\alpha_3 \dot{n}_z + \eta_1 v_{x,z}) \quad (17)$$

$$0 = -\gamma_1 \dot{n}_z + K_1 n_{z,zzz} + \Delta\chi H_z^2 n_z - \alpha_3 v_{x,z}. \quad (18)$$

The fastest growing solution is the one for which  $n_z$  is even in  $z$  with the form

$$v_x = A_1 z + A_2 \sin qz, \quad (19)$$

$$n_z = C_1 + C_2 \cos qz. \quad (20)$$

The distinctive feature of this solution is the presence of a  $k_z = 0$  mode (represented by a linear shear) whose rate of growth must be made equal to that of the periodic  $k_z \neq 0$  mode. It is also characterized by the peculiar fact that director rotations toward the magnetic field direction do not induce a fluid velocity in that direction.

To satisfy boundary conditions, the wave vector for the even solution must now satisfy

$$\frac{\tan P}{P} = \frac{h^2 - P^2 \eta}{h^2 - P^2} \quad (21)$$

where  $h = (\pi/2)(H_z/H_c)$ ,  $H_c = \pi(K_1/\Delta\chi)^{1/2}/d$ ,  $P = qd/2$  and  $\eta = \alpha_3^2/(\eta_b \gamma_1)$  while the rate, for both even and odd solutions, is

$$s = \frac{4 K_1 (h^2 - P^2)}{\gamma_1 d^2 (1 - \eta)}. \quad (22)$$

Since  $\eta$  is less than one, equation (21) has a solution in the range  $\pi/2 < P < \pi$ . It can be shown that the lowest order odd-symmetry solution has  $P = \pi$  so the even solution is always faster for this spatially uniform mode as it is for striped realignments discussed above.

The rate for the uniform solution is plotted with the rate for the periodic solution in figure 2a. For fields below  $(H/H_c)^2 \simeq 9.2$  the uniform solution is faster in MBBA. On the basis of this theory, which is only good for the small distortion limit, no stripes would be observed unless this field were exceeded. Beyond the linear regime however there may be spatially periodic solutions for small fields.

The rigid-boundaries results for  $k_x$  are compared with those of free boundaries in figure 2b. Apart from an upward shift in the critical field at which periodic structure emerges and slight shifts of wavelengths in the stripes, the exact solution for rigid boundaries is

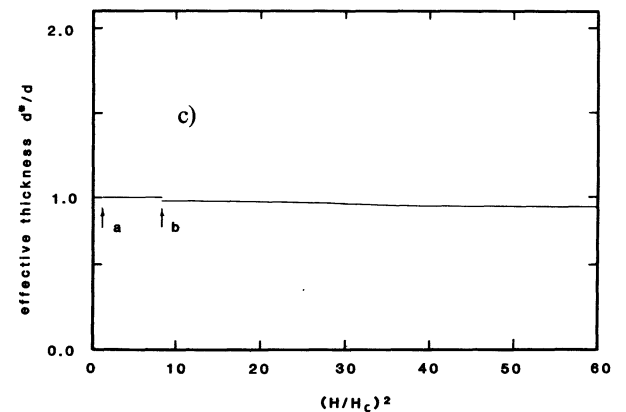
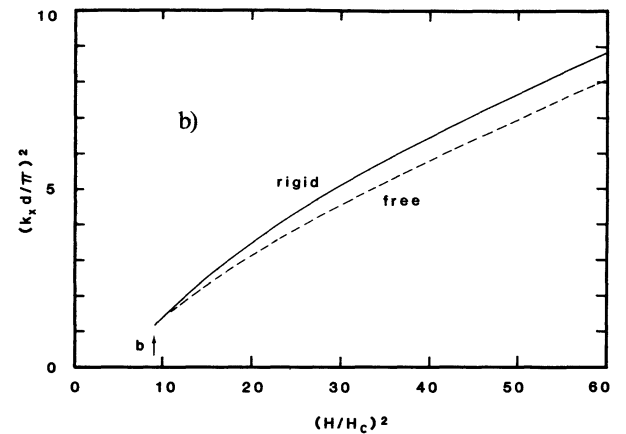
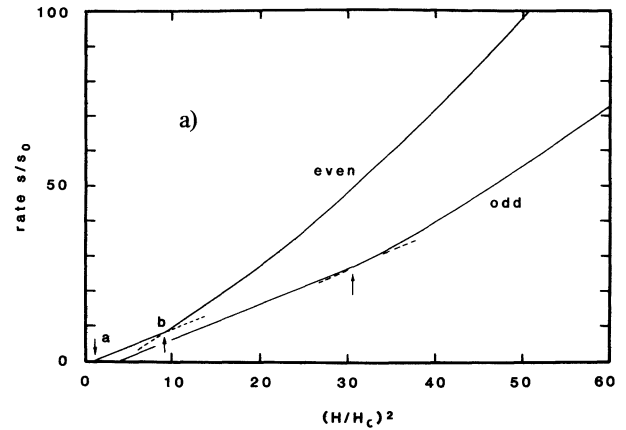


Fig. 2. — Analysis of two-dimensional case. (a) Rate of growth with rigid boundaries where  $s_0 = (\pi/d)^2 K_1/\gamma_1$ . Two regimes are present : for low fields above the Frederiks transition « a » the sample reorients by a spatially uniform mode without stripes whereas for high fields above « b » the striped instability is faster. Also, the even mode (even symmetry for  $n_z$ ) is faster than the odd mode. Parameters for MBBA were used :

$$K_1 = 5 \times 10^{-7} \text{ dyn}, K_2 = 3 \times 10^{-7} \text{ dyn},$$

$$K_3 = 8 \times 10^{-7} \text{ dyn},$$

$$\eta_a = 0.416 \text{ poise}, \eta_b = 0.248 \text{ poise}, \eta_c = 1.035 \text{ poise},$$

$$\gamma_1 = 0.763 \text{ poise}, \gamma_2 = 0.518 \text{ poise} [17].$$

(b) Comparison of periodicity of stripes along  $\hat{x}$  for rigid and free boundaries. That the stripes have similar wavelengths reflects the fact that the effective thickness is nearly  $d$  for rigid boundaries and even symmetry. (c) Effective thickness for even and odd modes with rigid boundaries.

essentially the same as for free boundaries. The reason for this is that for rigid boundaries the effective thickness differs little from  $d$ , its value for free boundaries, as shown in figure 2c. Mathematically one can see why the effective thickness remains constant by studying figure 3 showing the profile of the velocity parallel to the walls. Three independent modes combine in this solution, a free-boundaries-like mode, which has large transverse velocities at the walls, and two others, which decay exponentially from the walls and exactly cancel the first at the boundaries. The influence of the decaying modes is small in the bulk of the sample making the over-all behaviour much like the free-boundaries solution. They give rise to a large shear gradient confined to a boundary layer that is thinner the higher the driving field. This shear corresponds to a low viscosity process, being governed by  $\eta_b$ . At other places near the walls where the much larger elongational flow viscosity  $\nu_1$  is dominant, the decaying modes have less influence since the free-boundaries solution already satisfies rigid boundary conditions there and so the extra modes are not needed.

In the three-dimensional problem involving oblique stripes, a similar situation is expected : exponentially decaying modes fix up the free-boundaries solution in areas of the walls where the relatively small shear viscosities,  $\eta_a$ , and  $\eta_b$ , dominate. The extra shear flows remain a surface effect so that the over-all behaviour is that of the free-boundaries case.

We must emphasize that the reanalysis in this section of Guyon's model [5] for rigid boundaries has little to do with reality when the system responds with oblique stripes. When the stripes are not oblique (and this does occur [5]), or when there is uniform rotation with no stripes, these solutions are exact for the initial instability in the linearized limit.

**2.4 LONG-CHAIN LIMIT.** — An interesting case to consider is that of infinitely long and thin liquid crystal molecules. The macroscopic properties of long-chain systems have been studied theoretically [11] beginning with Onsager's work [12]. The splay elastic constant and several viscosities are expected to diverge : those

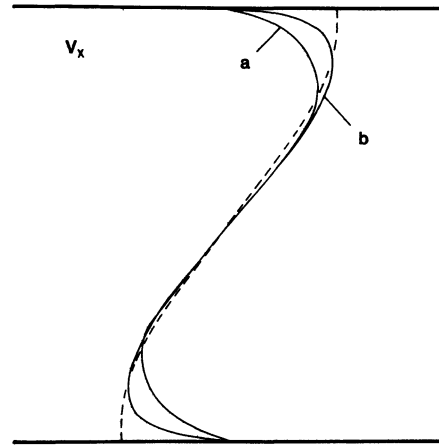


Fig. 3. — Velocity field  $v_x$  for exact rigid-boundaries solution of two-dimensional case with even symmetry for  $n_z$  at low field (a) and high field (b). The general solution (solid lines) is composed of three independent modes, one which is nearly identical to the free-boundaries solution (dotted line) and two others which decay exponentially from the boundaries. At higher driving fields (b), the first mode remains relatively unchanged and the other modes decay more rapidly giving rise to a greater shear gradient.

for pure rotation about molecular centres  $\gamma_1$ , for elongational flow  $\nu_1$ , and for shear across the chains  $\eta_c$ . Thus  $v_{x,x} = 0$ ,  $\nabla \cdot \mathbf{n} = 0$  and only twist-bend modes are allowed.

The Rayleigh dissipation function cannot contain infinite viscosities so it must be rewritten in order that large quantities cancel. Equations (5a) and (5b) for the torque can be written as

$$\dot{n}_y = -\frac{\alpha_2}{\gamma_1} v_{y,x} - \frac{\alpha_3}{\gamma_1} v_{x,y} + \frac{\Gamma_y}{\gamma_1} \quad (23a)$$

$$\dot{n}_z = -\frac{\alpha_2}{\gamma_1} v_{z,x} - \frac{\alpha_3}{\gamma_1} v_{x,z} + \frac{\Gamma_z}{\gamma_1} \quad (23b)$$

where  $\Gamma_y$  and  $\Gamma_z$  are the conservative torques from elasticity and the magnetic field. Replacing the director components in equation (2) by these expressions and dropping the elongational flow yields

$$R = \frac{1}{2} \left( \eta_b - \frac{\alpha_3^2}{\gamma_1} \right) (v_{x,y}^2 + v_{x,z}^2) + \frac{1}{2} \left( \eta_c - \frac{\alpha_2^2}{\gamma_1} \right) (v_{y,x}^2 + v_{z,x}^2) + \eta_a (v_{y,y}^2 + v_{z,z}^2) + \frac{1}{2} \eta_a (v_{y,z} + v_{z,y})^2 + \left( \eta_4 - \frac{\alpha_2 \alpha_3}{\gamma_1} \right) (v_{x,y} v_{y,x} + v_{x,z} v_{z,x}) + \frac{1}{2\gamma_1} (\Gamma_y^2 + \Gamma_z^2).$$

In the long-chain limit we set  $\gamma_1 = \eta_c \rightarrow \infty$  leaving

$$R = \frac{1}{2} \eta_b [(v_{x,y} + v_{y,x})^2 + (v_{x,z} + v_{z,x})^2] + \eta_a (v_{y,y}^2 + v_{z,z}^2) + \frac{1}{2} \eta_a (v_{y,z} + v_{z,y})^2. \quad (24)$$

Furthermore, from equations (23a) and (23b) the coupling between director rotation and flow is absolute

$$\dot{n}_y = v_{y,x} \quad (25a)$$

$$\dot{n}_z = v_{z,x}. \quad (25b)$$

Fluid flow along the director is possible as long as there are no gradients along  $\hat{x}$ . Since we seek a solution that is spatially periodic in both the  $x$  and  $y$  directions we must eliminate  $v_x$  altogether in  $R$ . This also eliminates the pressure. (Allowing the  $v_{x,y}$  and  $v_{x,z}$  terms to stay leads to a pure-twist structure.) Therefore, paying attention to (free) boundary conditions and fluid incompressibility, the expected solution is

$$\begin{aligned} v_y &= v_y \sin k_x x \sin k_y y \sin k_z z \\ v_z &= v_z \sin k_x x \cos k_y y \cos k_z z \\ n_y &= n_y \cos k_x x \sin k_y y \sin k_z z \\ n_z &= n_z \cos k_x x \cos k_y y \cos k_z z \end{aligned} \quad (26)$$

with  $k_z = \pi/d$ . One can verify that  $\nabla \cdot \mathbf{n} = 0$  as well.

The growth rate characteristic equation can be found directly from energy conservation. This leads to an analytic expression that can be readily explored in certain limits. The magnetic potential energy of the initially undistorted nematic sample decreases as the reorientational instability proceeds. This energy is either stored in elastic distortions or dissipated by viscous processes, a balance expressed as

$$\langle \dot{L} \rangle = \langle 2R \rangle, \quad (27)$$

since  $R$  is just one-half the dissipation energy density. The brackets indicate an integration over the sample volume as the energy balance is not point-by-point.

After some algebra, the effective viscosity emerges

$$\begin{aligned} \langle 2R \rangle &= \eta_{\text{eff}}(\dot{n}_y^2 + \dot{n}_z^2) = \\ &= \left[ \eta_b + \left( \frac{k_y^2 + k_z^2}{k_x^2} \right) \eta_a \right] (\dot{n}_y^2 + \dot{n}_z^2) \end{aligned} \quad (28a)$$

and the rate of change of potential energy is

$$\begin{aligned} \langle \dot{L} \rangle &= \left[ \Delta\chi H_z^2 - K_3 k_x^2 \left( \frac{k_y^2 + k_z^2}{k_y^2} \right) - \right. \\ &\quad \left. - K_2 \left( \frac{k_y^2 + k_z^2}{k_y^2} \right)^2 \right] n_z \dot{n}_z. \end{aligned} \quad (28b)$$

Finally, assuming a time dependence  $\exp(st)$ , the rate of growth is

$$s = \beta \frac{\Delta\chi H_z^2 \alpha - [K_3 \beta(1+\alpha) + K_2(1+\alpha)^2] k_z^2}{\eta_b \beta(1+\alpha) + \eta_a(1+\alpha)^2} \quad (29)$$

where  $\beta = (k_x/k_z)^2$  and  $\alpha = (k_y/k_z)^2$ .

This equation for the rate can be tailored for TMV liquid crystals by using the experimental fact that  $\alpha$  remains nearly constant for higher fields and that  $\beta$  is roughly linear in  $H_z^2$ . We have found by numerical

investigations of equation (29) that  $\eta_b$  must be small to account for the rapid jump  $\alpha$  makes from zero to two just above the threshold field and that  $K_2$  must be small to make  $\beta$  linear in  $H_z^2$ . With these adjustments, one finds by maximizing  $s$  with respect to  $\alpha$  and  $\beta$  the pleasing results

$$\alpha = 2 \quad (30)$$

independent of material parameters and

$$\beta = \frac{\Delta\chi H_z^2}{3 K_3 k_z^2}. \quad (31)$$

Thus  $\beta$  should depend linearly on  $H_z^2$  with a slope inversely proportional to  $K_3$ . The data from TMV samples exhibit both of the major features of this limit as will be described in more detail in the next section.

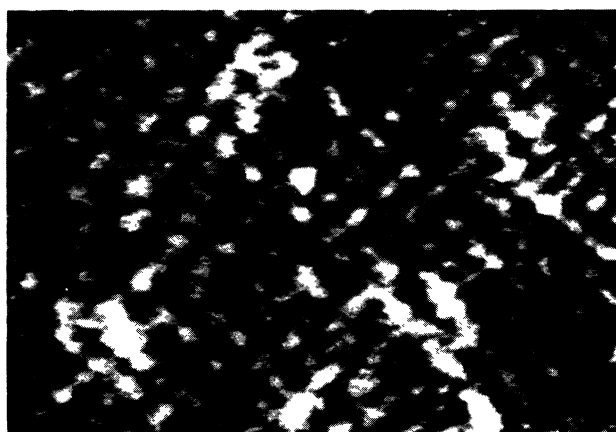
### 3. Experiments with TMV and MBBA.

Liquid crystals made of suspended tobacco mosaic virus have played an important part in liquid crystal physics, most notably the experiments which prompted Onsager to formulate his theory in 1942 for the nematic-isotropic phase transition in a rigid-rod fluid [12]. Since then TMV has remained for the most part in the structural biologist's laboratories. This neglect by liquid crystal physicists is probably due to the difficulty in handling these materials, especially in preparing well oriented, monodisperse samples for quantitative measurements. Our efforts in this area have succeeded to the point that we can now be confident that our TMV liquid crystals are indeed nematic (not gels or colloidal crystals), with well behaved elastic and viscous properties [2]. We have found these unusual nematics to be surprisingly attractive to work with. Perhaps the full potential of TMV as a model rigid-rod liquid crystal system will eventually be realized.

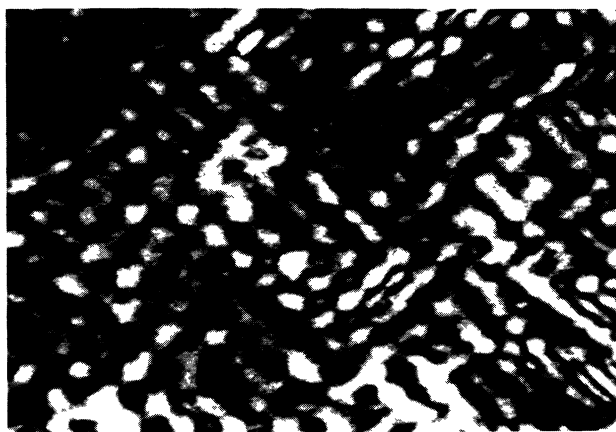
The virus particles were extracted from tobacco plants using the procedure described by Kreibig and Wetter [13], then suspended in water (borate buffered to pH 8.5 at an ionic strength of 50 mM) at a concentration of 148 mg/ml. Under these conditions the virus molecules are negatively charged, so their rigid-rod dimensions (180 Å in diameter and 3 000 Å long) are effectively increased by a cloud of counterions.

Parallel plate cells were fabricated from 0.5 in. dia. quartz windows, which had been coated with several hundred Ångstroms of silicon monoxide obliquely evaporated at 68° from the normal. The suspension was captured between the plates by a teflon washer of a given thickness and the whole assembly was held together with an aluminium clamp, making sure that the evaporation directions of the coatings were parallel. The TMV particles aligned parallel to the glass and perpendicular to the evaporation direction. Under the polarized microscope, well aligned samples exhibited characteristic streak-like fluctuations perpendicular to the director.

Four samples were prepared with thicknesses of 90, 201, 297 and 366  $\mu\text{m}$ . After annealing in a large magnetic field for a few minutes, a sample was exposed to a known field normal to the cell for 20 seconds to several minutes in order to create a striped pattern as in figure 4. The pattern was then photographed through a microscope. Measurements of the angle and perpendicular spacing between stripes were taken directly from the negatives, converted to the wave vectors  $k_x$  and  $k_y$ , parallel and perpendicular to the director, respectively, then plotted in figure 5. Comparisons with the theoretical curves in figure 5 will be described in section 4. Several of the measurements were checked by comparing to measurements taken from optical Fourier transforms as seen in figure 4.



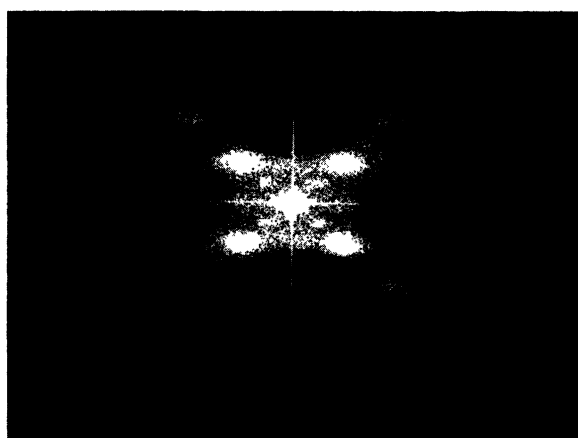
a)



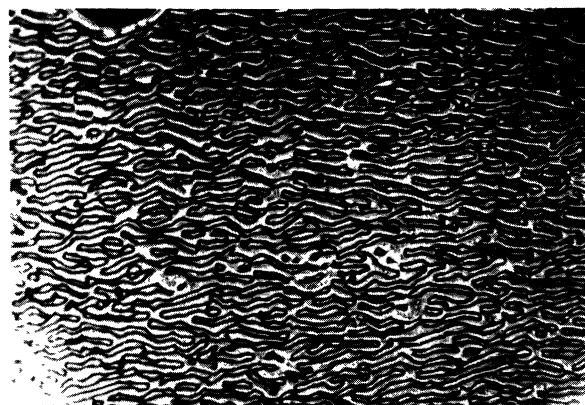
b)



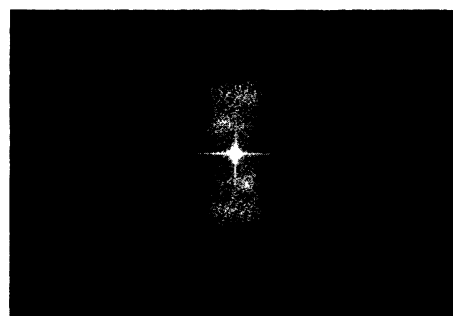
c)



d)



e)



f)

Fig. 4. — Time development sequence of transient periodic structures in tobacco mosaic virus nematic liquid crystal. The sample was initially aligned in the plane of the sample along  $\hat{n}$  and the magnetic field was applied normal to the sample as shown in figure 1. Under crossed polarizers the distortion is first seen as a cross-hatching of light and dark patches which eventually connect to form oblique stripes. Time of exposure to the field : (a) 20 s, (b) 40 s. (c) Well developed structure. The distance between stripes is 50  $\mu\text{m}$ . (d) Optical diffraction pattern of (c). This shows that the spatial Fourier transform of the stripes consists of well developed periodicities  $k_x$  and  $k_y$  along with less intense period doubling peaks owing to a pairing-up in the annealing process. (e) and (f) Oblique stripes and Fourier transform in MBBA. Rapid annealing occurs in the first few seconds resulting in less definition and more pairing-up.

Finally, an effort was made to photograph the instability in MBBA; the best result is seen with its optical Fourier transform in figures 4e and 4f. Unfortunately the fast relaxation time of this material prevented capturing the initial distortion on film, although the obliquely striped pattern in figure 4e is unmistakable in spite of the extensive annealing that had already taken place in the first second or so of the transition. The pairing and subsequent annihilation of adjacent defects was a common mode of annealing observed in both TMV and MBBA samples. It is manifest in the optical Fourier transforms as a period doubling spot appearing between primary maxima in figures 4d and 4f.

#### 4. Discussion.

**4.1 OBLIQUENESS OF STRIPES.** — In order to explore the predictions of the model for the oblique stripes, the characteristic equation (Eq. (11)) was numerically solved for the maximum rate of growth at a given field by varying  $k_x$  and  $k_y$ , while assuming an effective thickness of  $d$  (therefore  $k_z = \pi/d$ ) and using MBBA viscosities and elastic constants. The first aspect of the solution to notice is that oblique stripes appear for fields  $H$  greater than about  $1.5 H_c$  and less than  $5 H_c$ .

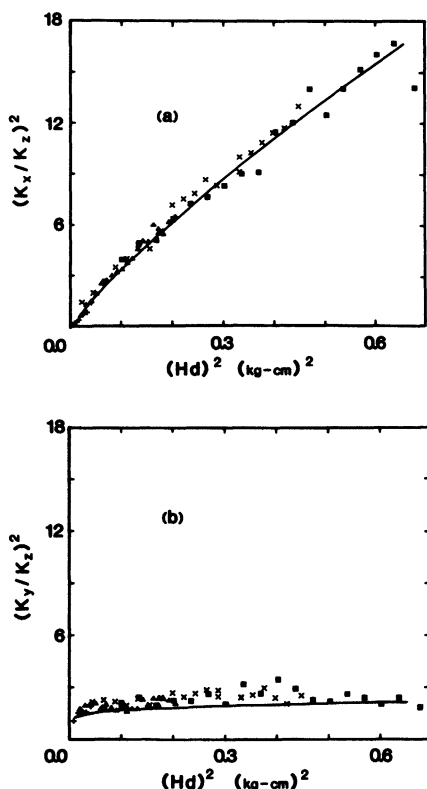


Fig. 5. — Measured wave vectors in TMV as function of field, and theoretical curves from free boundaries model. The wavelengths and angles of the stripes in four different thickness samples were taken from photographs and converted to  $k_x$  and  $k_y$ . The curves were generated from equation (11) using viscosities and elastic constants similar to those predicted for long, hard-rod liquid crystals.

Below this range there is a spatially uniform mode of reorientation and above this range there are stripes but they are not oblique: the system chooses the two-dimensional mode which has been discussed in section 2.3. We know that this latter instability is essentially a bend mode, polarized in the  $x$ - $z$  plane (that is, only the  $z$ -component of the director varies sinusoidally with  $x$ ), with some splay involved owing to the presence of boundary conditions. The important point is that the obliqueness comes in continuously as the field strength is decreased. This suggests that there is a continuous change in the bend mode from higher fields with straight stripes to lower fields with oblique stripes.

Under crossed polarizers, the distortion represented by  $n_y$  and  $n_z$  in equation (13) would have the correct characteristic cross-hatched pattern that is observed in our samples; it is the superposition of two oblique sets of « rolls » which we may analyse separately. One roll is given by

$$n^{(1)} = \left(1, \frac{1}{2} D \sin(k_x x + k_y y) \sin(k_z z), \frac{1}{2} E \cos(k_x x + k_y y) \cos(k_z z)\right) \quad (32)$$

and the other by  $k_y \rightarrow -k_y$ . At a constant  $y$  and  $z$ , we see from equation (32) that the director lies on the surface of a cone with an elliptical base and that it precesses around this in a helicoidal fashion with increasing  $x$ . Why does the linearly polarized bend mode, favoured at higher fields, become elliptically polarized at lower fields? By comparing the distortion energies of these two cases it becomes evident that the bend mode can avoid splay by becoming elliptically polarized. It is helpful to think of the rolls in equation (32) as a superposition of linearly polarized bend modes that are both tilted (from lying in the  $x$ -plane) and « staggered » or « sheared » (in the  $x$ - $y$  plane) although such modes no longer satisfy the equations of motion individually. The splay energy of one roll is

$$F_{\text{splay}} \sim \frac{1}{2} K_1 (Dk_y - Ek_z)^2. \quad (33)$$

The term  $Ek_z$  is present because of boundary conditions whereas  $Dk_y$  derives from tilting the « sheared » bend modes. In equation (33) we see that the splay energy can be reduced by tilting (increasing  $D$ ) a sheared bend mode characterized by  $k_y$ . Thus we see that the oblique, cross-hatched structure, made up of sheared and tilted bend modes, allows the system to avoid splay at some cost in twist energy. In fact, for systems that strongly avoid splay, we would expect to have  $k_y$  proportional to  $k_z$  as in the long-chain limit (Eq. (30)).

Arguments based only on the elastic energy are of course incomplete since viscosities can have even larger effects on the rate of growth and on the oblique angle than can the elastic constants. The viscosity anisotropy tends to be larger than the elastic anisotropy in liquid crystals so the rates of growth for different distortions can be quite dissimilar. In order

to determine which viscosities are important, we returned to the numerical solution to the free-boundaries model, equation (11), and changed the viscosities to see what happens to the stripes. On  $k_x$  none of the viscosities have much effect, indicating that this periodicity is mediated almost entirely by the bend elastic restoring force (Fig. 6a). On the other hand, the  $k_y$  periodicity is greatly affected by changes in viscosities, notably  $\eta_b$  and  $\nu_1$ . Specifically, a smaller  $\eta_b$ , which is the viscosity for elongated molecules sliding longitudinally past one another, tends to make  $k_y$  more constant with respect to field whereas a greater elongational flow viscosity  $\nu_1$  tends to increase  $k_y$  for all values of the field (Fig. 6b).

Comparing the dissipation functions for a linearly polarized bend-splay mode, which gives perpendicular stripes, and the helicoidal, elliptically polarized modes, which give oblique stripes, we find that perhaps the most important difference is in the elongational flow term. Similar to splay, elongational flow can be at least partly avoided in the helicoidal structure since the flow along  $\hat{x}$  can « escape » toward  $\hat{y}$  and  $\hat{z}$ . The pertinent term in the dissipation function is

$$\nu_1 v_{x,x}^2 = \nu_1 (v_{y,y} + v_{z,z})^2 \sim \nu_1 (k_y B - k_z C)^2. \quad (34)$$

The recipe for fast growth is to decrease the field energy as quickly as possible, transferring the energy to elastic distortions by the smallest viscosity routes available. By becoming oblique, the stripes lower the field energy more quickly than perpendicular stripes since elongational flow can be traded for other flows.

When the driving field is high enough, the avoidance of splay and elongational flow is not important enough to favour the oblique stripes of the helicoidal structure over the perpendicular stripes of the bend-splay structure (Figs. 6a and 6b). The system takes the most direct route toward aligning with the field, which is the bend-splay mode. The elongational flow and splay are confined to an increasingly thin boundary layer at high fields so that the pure bend in the bulk becomes the only important distortion. Moreover, it is likely that the overall effective viscosity is no longer lowered by trading elongational flow for transverse flow since the  $\eta_c$  term in equation (2) must grow as the field increases. This transition from oblique to perpendicular has been observed in MBBA, which is of relatively low molecular weight : figure 4e shows oblique stripes observed at low reduced field in our laboratory but reference [5] discusses measurements taken from perpendicular stripes in thick samples and hence high reduced field. Our samples were too thin to drive them into the perpendicular regime since this requires very high fields leading to very fast annealing of the transient structures. In high molecular weight nematics such as TMV the oblique regime is quite extended in field. We are not aware of any observations of strictly perpendicular stripes in such systems although it is possible that in thick samples they would be seen.

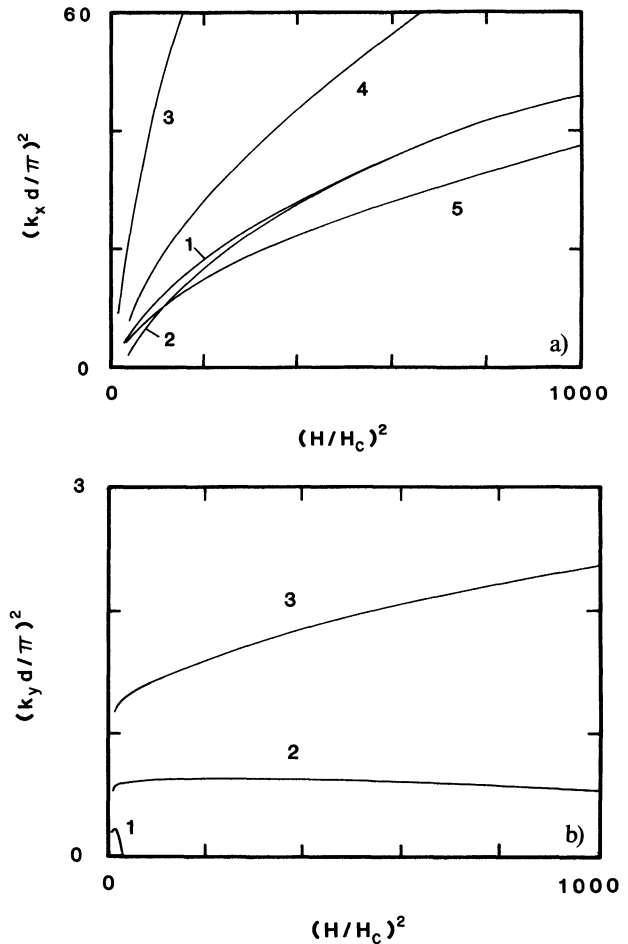


Fig. 6. — Effects of changing material parameters on stripes in three-dimensional model, equation (11). (a) Curve 1 shows the values taken by  $k_x$  as a function of field for MBBA viscosities and elastic constants. Increasing the splay elastic constant  $K_1$  by a factor of 10 (curve 2) has little effect apart from shifting the critical field; similarly,  $K_2$  (twist) has little or no effect on  $k_x$  (not shown). Decreasing  $K_3$  (bend) by a factor of 10, however, has a large effect (curve 3) as does decreasing the shear viscosity  $\eta_b$  by a factor of 2 (curve 4), whereas halving  $\nu_1$ , the elongational flow viscosity, has relatively little effect (curve 5). This shows that the periodicity along the initial director is governed by bend modes, which dominate the bulk of the sample, while splay and elongational flow being confined to thin layers near the surfaces have less influence as the bend mode wavelength becomes much smaller than the sample thickness. (b) The periodicity  $k_y$ , normal to the director is especially sensitive to viscosities and the twist elastic constant. Curve 1 shows  $k_y$  for MBBA, indicating that the stripes are oblique only for low fields  $(H/H_c)^2 \leq 25$ ; increasing  $K_2$  causes the stripes never to be oblique (not shown). Decreasing  $\eta_b$  by a factor of 10 (curve 2) greatly extends the range of fields in which the stripes are oblique, and makes  $k_y$  relatively constant; simultaneously increasing  $\nu_1$  by a factor of 10 (curve 3) tends to increase  $k_y$  further. These trends reflect the expected behaviour of hard-rod liquid crystals.

4.2 HARD ROD PARAMETERS. — We have analysed the measurements of the in-plane wave vectors, shown in figure 5, for the elasticity and viscosity parameters in light of the models for long, hard-rod

Table I. — *Elasticity and viscosity ratios for theoretical hard rod and long-chain models compared with MBBA and with TMV fitting parameters from this work. The standard order parameter is  $S$  and the chain length is  $L$ .*

Ratio	Hard Rod Theory		Long Chain Theory (°)		MBBA (d)	TMV
	General	$S = 0.80$	General	$L \rightarrow \infty$		
$K_2/K_1$	$\frac{1}{3}$	0.33 (a)	$L^{-1}$	0	0.6	0.22
$K_3/K_1$	—	6.3 (a)	$L^{-1}$	0	1.6	8.8
$\eta_a/\eta_c$	$\frac{(1-S)(2+S)}{2(1+2S)^2}$	0.041 (b)	$L^{-2}$	0	0.40	0.040
$\eta_b/\eta_c$	$\left(\frac{1-S}{1+2S}\right)^2$	0.0059 (b)	$L^{-2}$	0	0.24	0.015
$\gamma_1/\eta_c$	$\frac{3S}{(1+2S)^2}$	0.36 (b)	$\alpha L^2/L^2$	finite	0.41	0.95
$\nu_1/\eta_c$	$\frac{(1+2S-S^2)(2+S)}{6(1+2S)^2}$	0.14 (b)	$\beta L^2/L^2$	finite	0.50	0.21

(a) Reference [14].

(b) Reference [15].

(c) Reference [11].

(d) Reference [7].

and infinite-chain liquid crystals. There exist theoretical ideas for the relative magnitudes of elastic constants [11, 14] and viscosities [11, 15] of such nematics; a comparison of values is made in table I along with measured values for MBBA and the fitting parameters for the data in figure 5. The fitting procedure was not a least-squares type; instead we searched for consistency between these data and some similar data from twist-bend instability experiments with the same TMV samples [2]. The numbers we obtained for our TMV samples must be taken as qualitative, but certain conclusions seem inescapable.

The results indicate a much higher anisotropy in the elastic and viscous properties of our TMV nematic samples than is found in a typical thermotropic nematic such as MBBA. It is interesting to see that the extreme limit of the infinite chain model ( $K_1$ ,  $\gamma_1$ ,  $\nu_1$  and  $\eta_c$  all infinite) plus the assumption of vanishingly small  $K_2$  and  $\eta_b$  gave a good description of the high field data on TMV. However, much less extreme sets of parameters also fit the data very well, so the infinite chain limit is not necessarily relevant. In fact,  $K_3 > K_1 > K_2$  seems to be a reasonable ordering of the elastic moduli, in agreement with hard rod theory of the nematic phase. The relative magnitudes of the viscosities needed to fit the data are also consistent with hard rod theory. Further refinement of theoretical models and more extensive data will be necessary before more exact conclusions can be reached.

## 5. Conclusions.

Magnetic reorientational instabilities appear to be quite common and easy to observe in lyotropic nematic liquid crystals. We would expect a similar class of phenomena in cholesteric liquid crystals as well. The analysis of these cases should follow the lines of thought presented here for the somewhat nontrivial splay-bend geometry. Our analysis has shown how the obliqueness of the observed stripes is a consequence of the high anisotropy found in rigid rod and polymer based nematics, as opposed to the less anisotropic materials, like MBBA. We've also seen that there is useful information to extract from the configuration and dimensions of the stripes that occur; whether such measurements could be refined to a routine for characterizing the mechanical properties of liquid crystals remains to be seen. It is significant however that a greater or lesser number of mechanical parameters come into play as the geometry is varied by changing the direction of the applied field and as the field strength or sample thickness is varied. This provides an opportunity to make a more complete and less ambiguous set of measurements than we have so far performed.

## Acknowledgments.

It is a pleasure to thank Professor Donald Caspar and his assistant Marguerite Cahoon of the Rosentiel Basic Medical Sciences Research Center at Brandeis

University for kindly supplying tobacco mosaic virus suspensions and for their interest. We have benefited greatly from discussions with Henk Lekkerkerker, Hiap Ong, Frank Leslie and Michael Cross.

Financial support was provided by the NSF through grant number DMR-8210477 and by the Martin Fisher School of Physics at Brandeis University.

#### References

- [1] LONBERG, F., FRADEN, S., HURD, A. J. and MEYER, R. B., *Phys. Rev. Lett.* **52** (1984) 1903.
- [2] FRADEN, S., HURD, A. J., MEYER, R. B., CAHOON, M. and CASPAR, D. L. D., Proceedings of the Les Houches *Workshop on Colloidal Crystals*, February, 1984, to be published by Les Editions de Physique.
- [3] CHARVOLIN, J. and HENDRIKX, Y., *J. Physique Lett.* **41** (1980) L-597.
- [4] YU, L. J. and SAUPE, A., *J. Am. Chem. Soc.* **102** (1980) 4879.
- [5] GUYON, E., MEYER, R. B. and SALAN, J., *Mol. Cryst. Liq. Cryst.* **54** (1979) 261.
- [6] CARR, E. F., *Mol. Cryst. Liq. Cryst.* **34** (1977) L-159.
- [7] CHANDRASEKHAR, S., *Liquid Crystals* (Cambridge University Press, Cambridge) 1977.
- [8] VERTOGEN, G., *Z. Naturforsch.* **36A** (1983) 1273.
- [9] GOLDSTEIN, H., *Classical Mechanics* (Addison-Wesley, Reading) 1950, p. 21 and p. 232.
- [10] PIERANSKI, P., BROCHARD, F. and GUYON, E., *J. Physique* **34** (1973) 35.
- [11] MEYER, R. B., in *Polymer Liquid Crystals*, edited by A. Ciferri, W. R. Krigbaum and R. B. Meyer (Academic Press, New York) 1982, Chap. 6.
- [12] ONSAGER, L., *Ann. N.Y. Acad. Sci.* **51** (1949) 627.
- [13] KRIEBIG, U. and WETTER, C., *Z. Naturforsch.* **35C** (1980) 750.
- [14] STRALEY, J. P., *Phys. Rev. A* **8** (1973) 2181.
- [15] MARUCCI, G., *Mol. Cryst. Liq. Cryst.* **72L** (1982) 153 L.
- [16] DE GENNES, P. G., in *Polymer Liquid Crystals*, edited by A. Ciferri, W. R. Krigbaum and R. B. Meyer (Academic Press, New York) 1982, Chap. 5.
- [17] DE GENNES, P. G., *The Physics of Liquid Crystals* (CLARENDON PRESS, OXFORD) 1975.